Supporting Information for

Investigating Polymer Infiltration Kinetics in Nanoporous Metal Scaffolds Using UV-Vis Spectroscopy

Weiwei Kong[1*], Chuyi Pan[1,2*], Rongyue Lin[1], Mengjie Fan[3], John M. Vohs[3], Russell J. Composto[1]

1: Department of Materials Science and Engineering, University of Pennsylvania, Philadelphia, PA
2: Department of Chemistry, University of Pennsylvania, Philadelphia, PA
3: Department of Chemical and Biomolecular Engineering, University of Pennsylvania, Philadelphia, PA

*: Those authors contributed equally to this project

Atomic Force Microscopy and Image Analysis

Tapping mode AFM was performed using Bruker Icon AFM with non-contact tips (TAP300AL-G-50 radius of curvature < 10 nm, Ted Pella). Image analysis was performed using Gwyddion software. The images were leveled using mean field subtraction function. Background noise was removed using a 2nd order polynomial background. Autocorrelation functions were performed on 1 x 1 μm^2 images with filters and background subtraction as described above.

Height Image

Figures S1-S3 show the AFM height images of the NPG composites at various stages of infiltration with various molecular weights. For as-cast NPG, the ligament structure was visible, with a constant pore diameter of around 100 nm. The as-cast composites displayed high surface roughness (~10-15 nm), whereas fully infiltrated NPG composite with P2VP displayed low surface roughness (~2-3 nm). The bi-continuous structure was also invisible in the fully infiltrated composites. Similarly, the height of the as-cast composite had a large range, whereas the fully infiltrated material had a small range for height. We interpret this phenomenon as polymer has filled all pores to the surface. The infiltration for each material involved thermal annealing at 140 °C for various times, followed by quenching on a metal plate to room temperature. Table 1 below shows the infiltration time for each P2VP molecular weight. We note that this characterization method only probes the surface of the NPG film, and hence cannot provide information on the remainder of the composite, (e.g., if the polymer has filled half of the pore).

Table 1. P2VP Mw and their full infiltration time

Sample	100 % Infiltration Time
P2VP-79	10 min
P2VP-277	5 hours
P2VP-547	5 hours
P2VP-855	17 hours

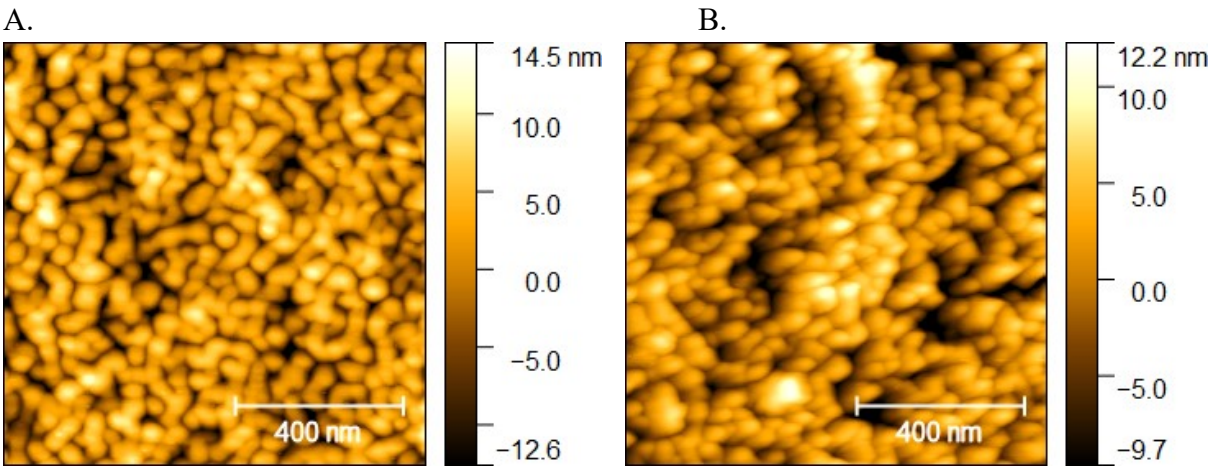

Figure S1: (A) AFM height image of as-cast P2VP-79:NPG composite. (B) Height image of fully infiltrated P2VP-79:NPG composite.

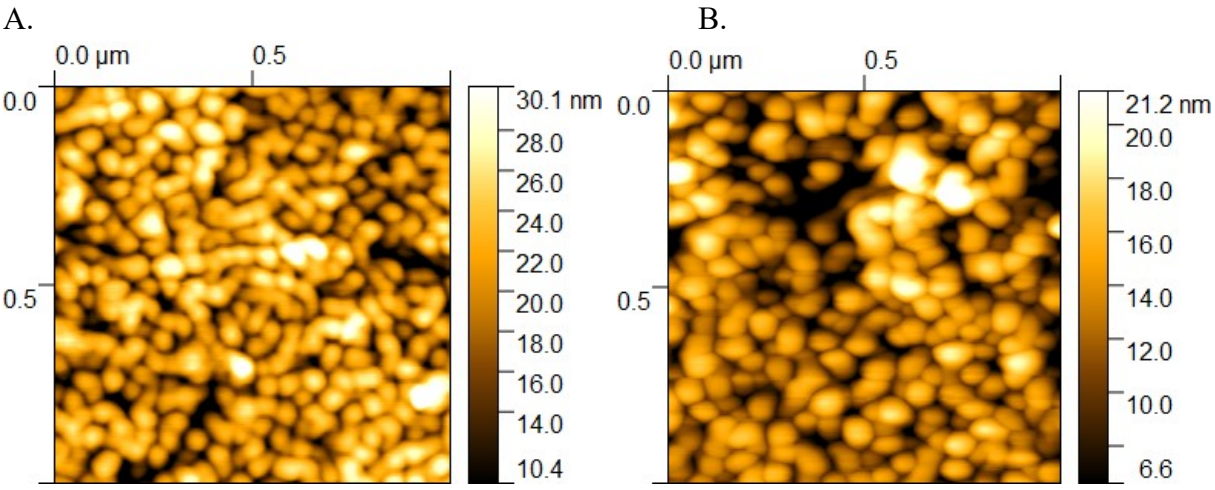

Figure S2: (A) AFM height image of as-cast P2VP-277:NPG composite. (B) Height image of fully infiltrated P2VP-277:NPG composite.

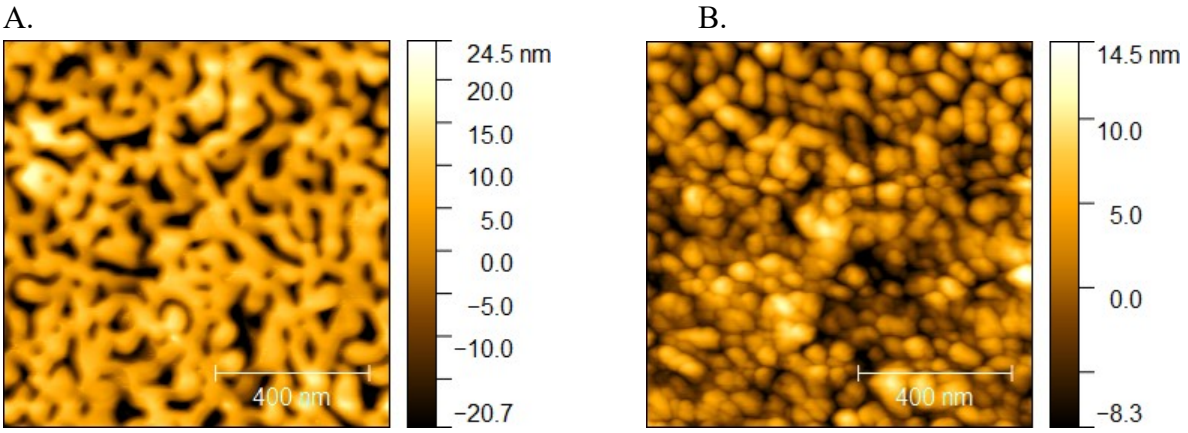

Figure S3: (A) AFM height image of as-cast P2VP-855:NPG composite. (B) Height image of fully infiltrated P2VP-855:NPG composite.

Phase Image

Figures S4-S7 show the AFM phase images of the NPG composites at various stages of infiltration with various molecular weights. For as-cast NPG, the ligament explored a high difference in degrees, indicating a significant phase lag from tapping hard materials. The fully infiltrated surface had lower difference in degrees, which showed that polymers have filled the pores, and potentially wets the gold surface as the tip explored smaller phase lag when tapping soft surfaces.

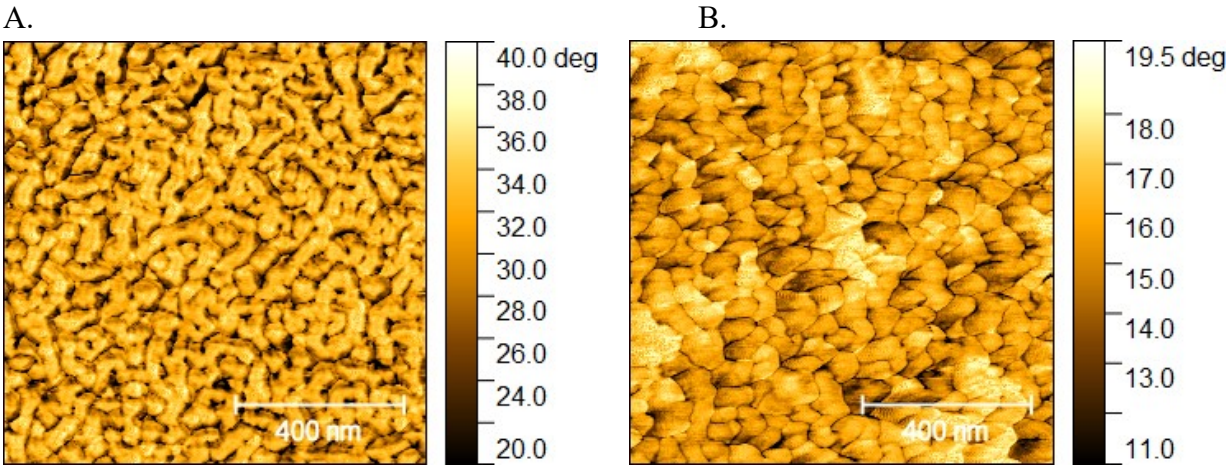

Figure S4: (A) AFM phase image of as-cast P2VP-79:NPG composite. (B) Phase image of fully infiltrated P2VP-79:NPG composite.

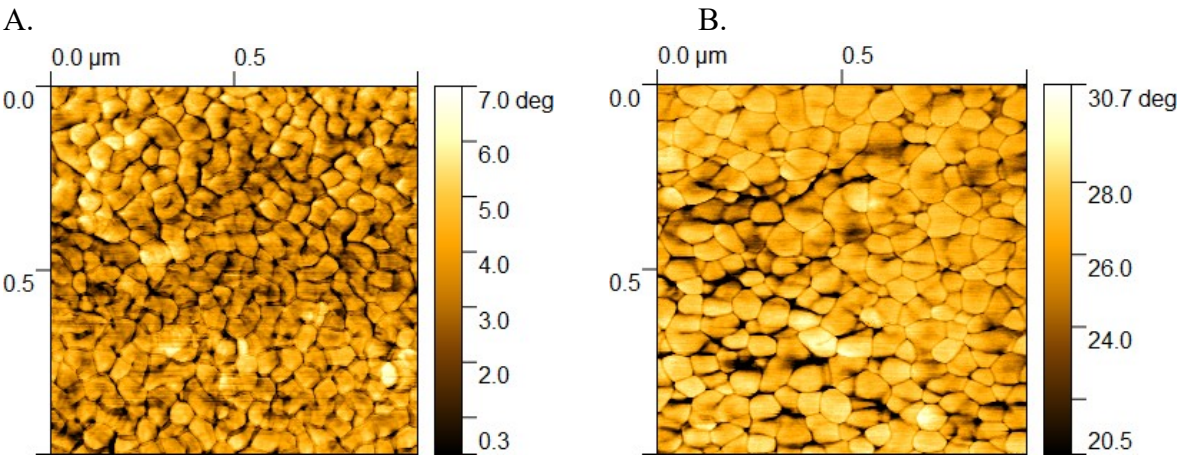

Figure S5: (A) AFM phase image of as-cast P2VP-277:NPG composite. (B) Phase image of fully infiltrated P2VP-277:NPG composite.

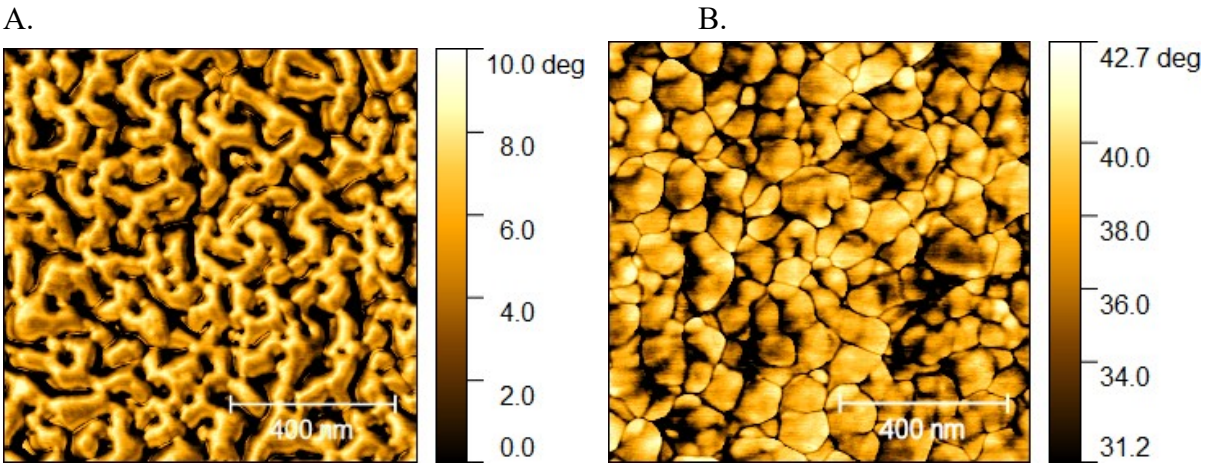

Figure S6: (A) AFM phase image of as-cast P2VP-547:NPG composite. (B) Phase image of fully infiltrated P2VP-547:NPG composite.

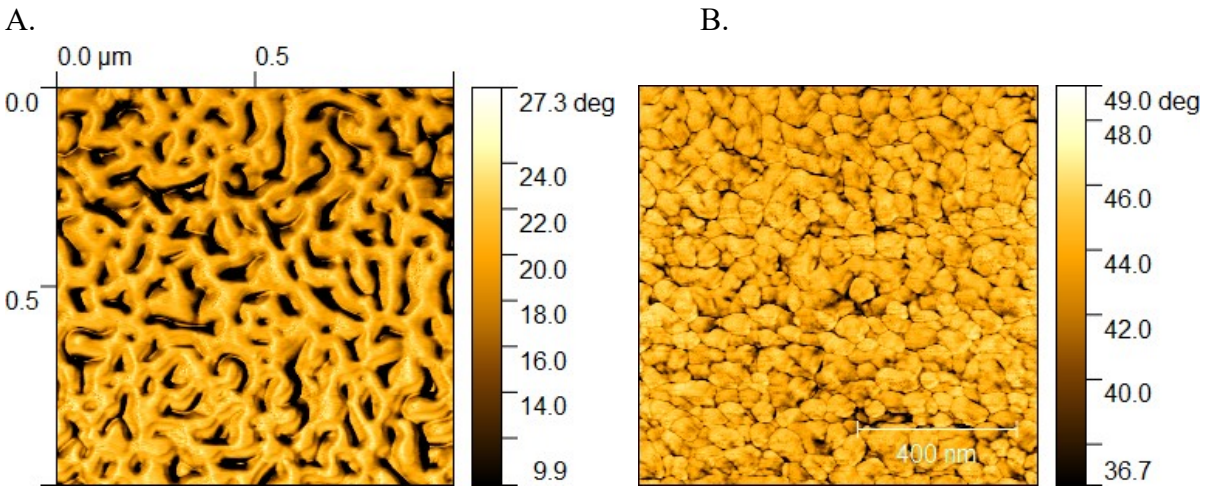

Figure S7: (A) AFM phase image of as-cast P2VP-855:NPG composite. (B) Phase image of fully infiltrated P2VP-855:NPG composite.

Surface Wetting Properties

Figure S8 shows the phase image of the water contact angle (WCA) of PS filled NPG composite and P2VP filled NPG composite. Each contact angle was an average of three measurements. As the contact angle is between gold's contact angle (65°) and PS contact angle (90°), we are certain that PS does not wet the surface yet forms a mushroom-like formation on the NPG surface. The P2VP filled composite's contact angle is similar to that of pure P2VP (67°). We acknowledge that since P2VP's WCA is similar to that of gold, WCA alone is not sufficient in proving the surface wetting property of P2VP. However, by combining the phase image data, we can infer this property.

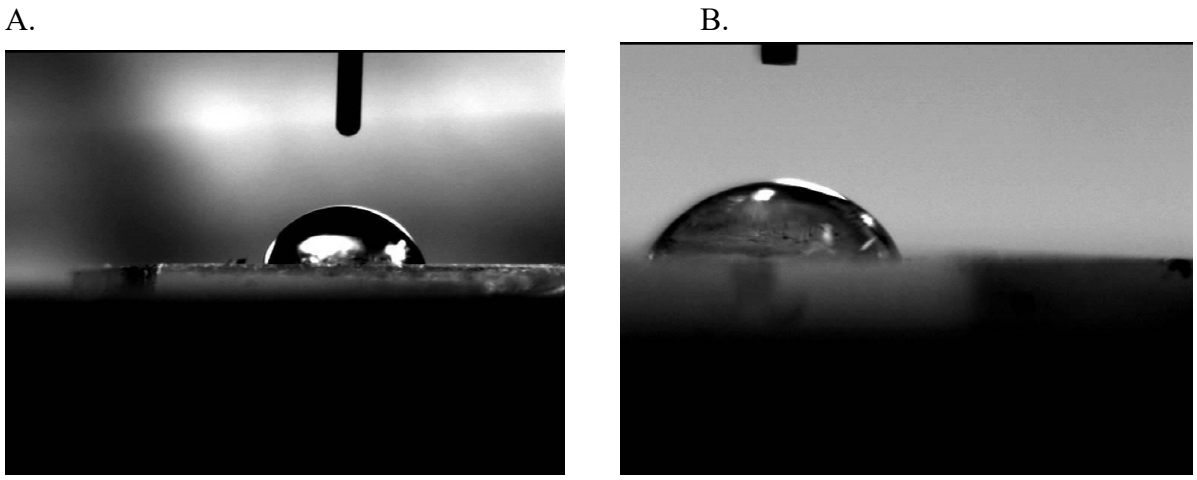

Figure S8: (A) WCA of PS filled composite, angle = 70.4 °. (B) WCA of P2VP filled composite, angle = 63.3°.

UV-Vis Measurements of Absorbance

Absorbance spectra of the glass substrate and the different polymer thin films were taken using Varian Cary Win 5000 UV-VIS-NIR Spectrophotometer with wavelengths ranging from 200-1000 nm. Figure S9 below shows the absorbance spectra of the different substrates.

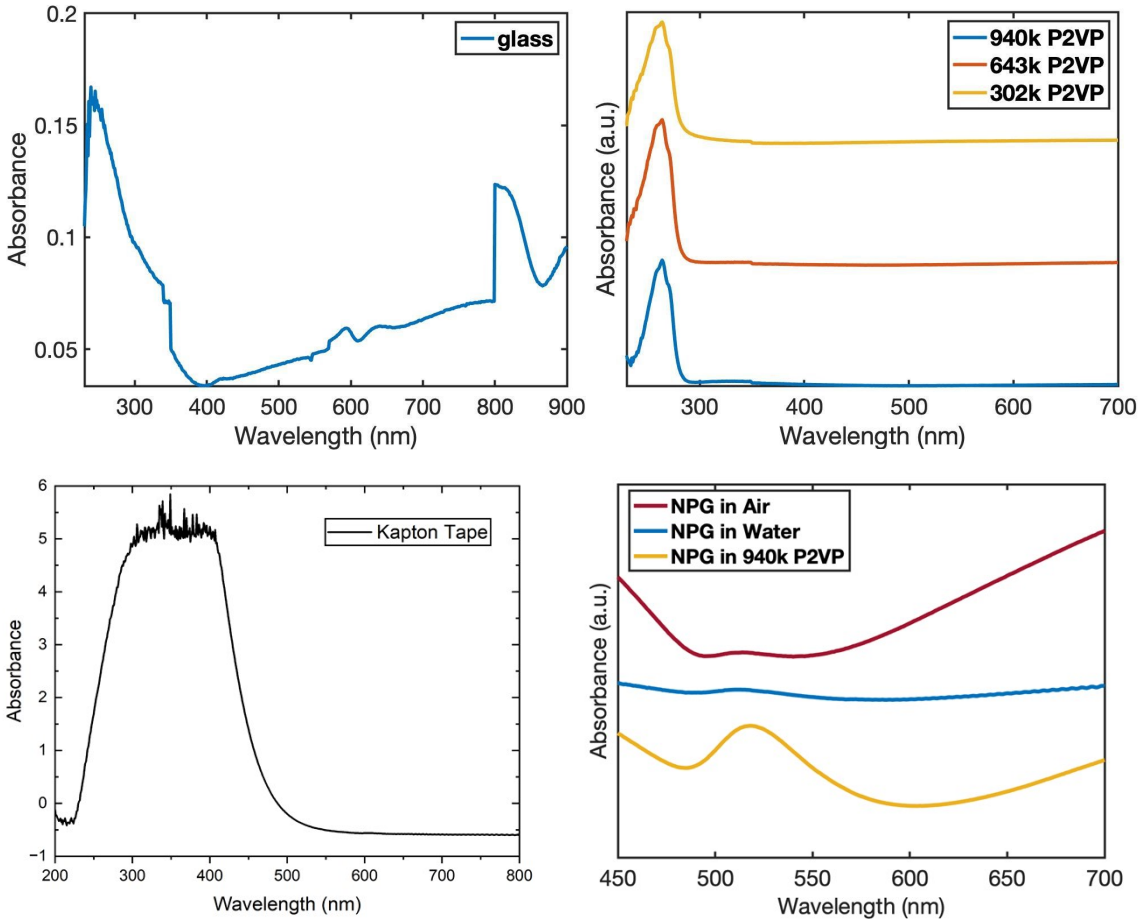

Figure S9: Absorbance spectra of the glass substrate, different P2VP thin films and tape.

Absorbance spectra of each composite at different infiltration times were taken using Varian Cary Win 5000 UV-VIS-NIR Spectrophotometer with wavelengths ranging from 200-1000 nm. Each polymer composite's spectrum was taken from as-cast to full infiltration, with various time intervals in between. All polymer molecular weights have been used to test absorbance for 3 trials. The spectra showed a rightwards shift of the resonance peak, indicating that the refractive index of the material has changed at various stages of infiltration. We could then utilize the absorbance spectra to determine infiltration kinetics. Figure S10 below shows the absorbance spectra of different P2VP composites.

P2VP-79

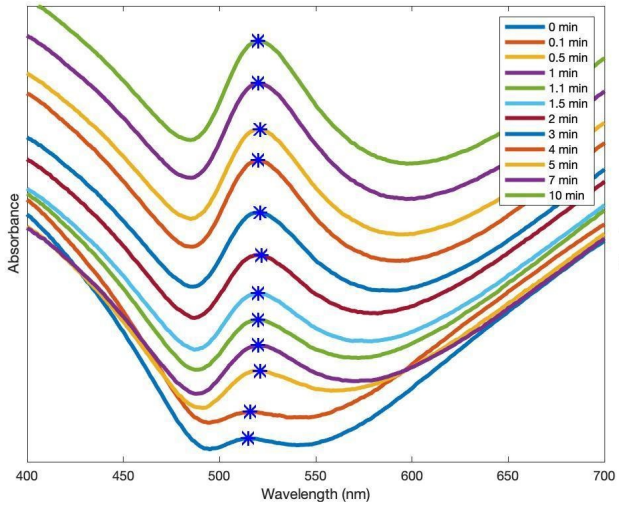

P2VP-277

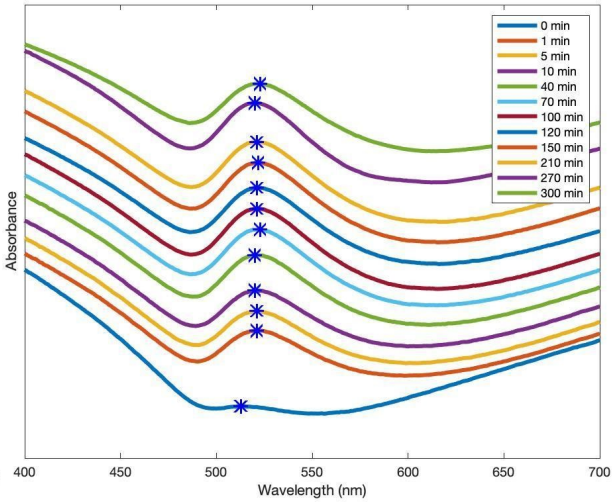

P2VP-855

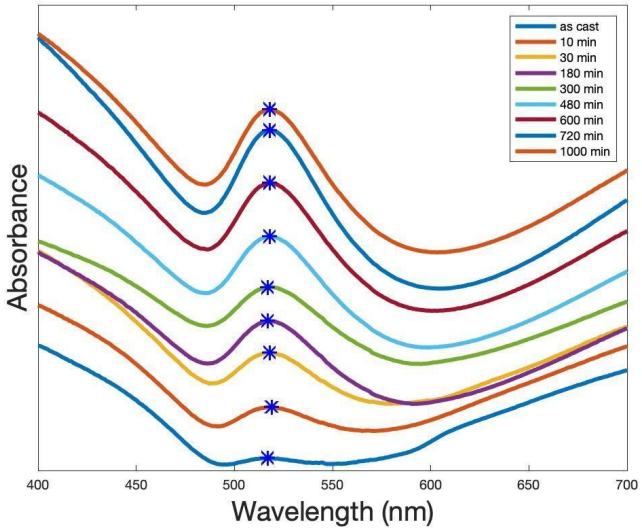

Figure S10: Absorbance spectra of different P2VP-NPG composites.

P2VP Infiltration Kinetics

It is also worth noting that as P2VP infiltrates into the pores, the absorbance increases, the peak width gets wider and therefore, the peak area gets larger. To determine infiltration kinetics, all three variables have been plotted against infiltration time, as shown in Figure 11, and the infiltration kinetics was determined using MATLAB curve fitting software. Figure S12 shows the infiltration extent vs time from all three variables. The 80% infiltration time is similar from each of the three methods (~3% difference), indicating that the usage of any variable to determine infiltration kinetics is acceptable. For best simplification, we used peak height vs time for all P2VP composites.

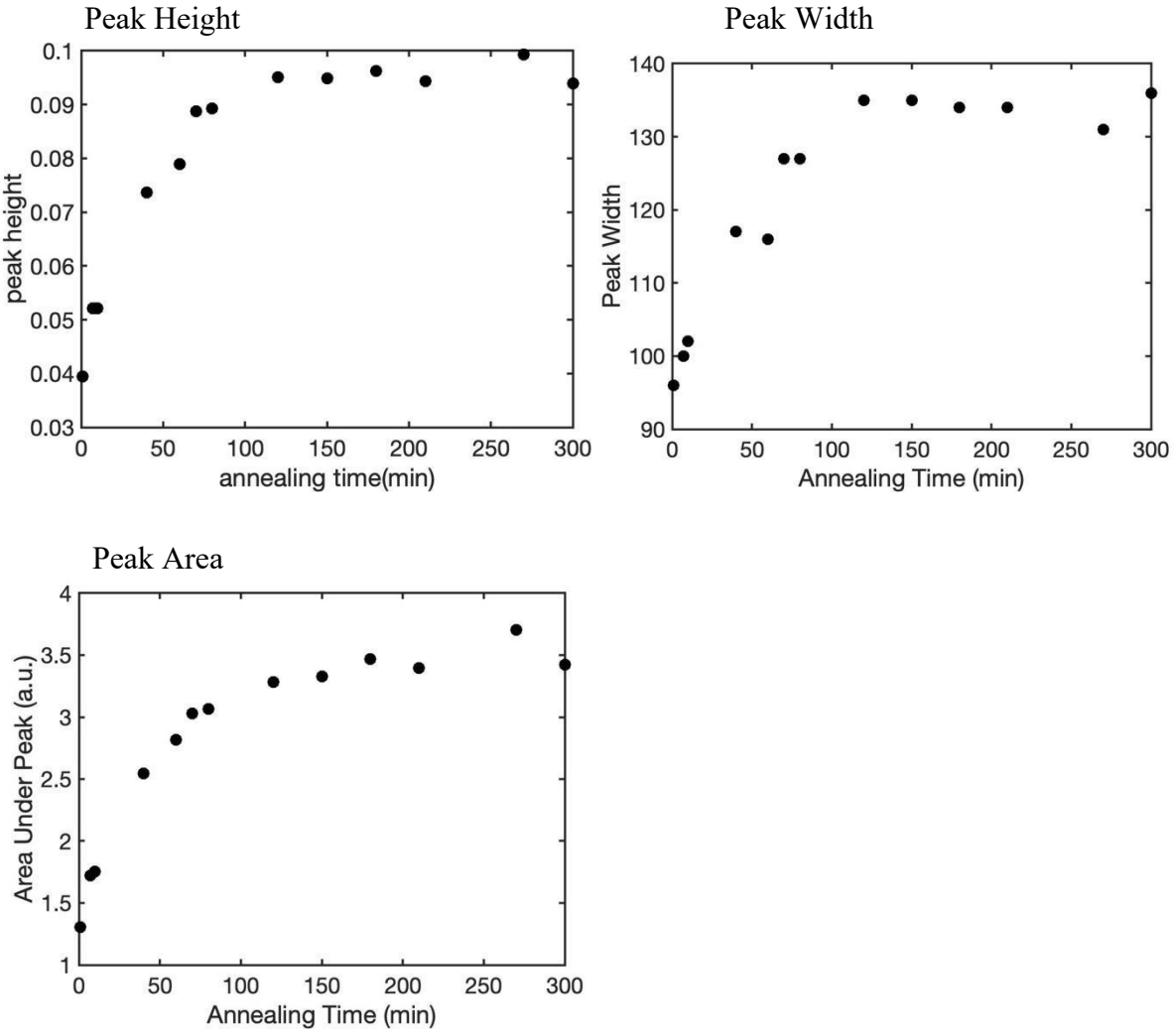

Figure S11: Peak height, width and area vs time for P2VP-547 composite.

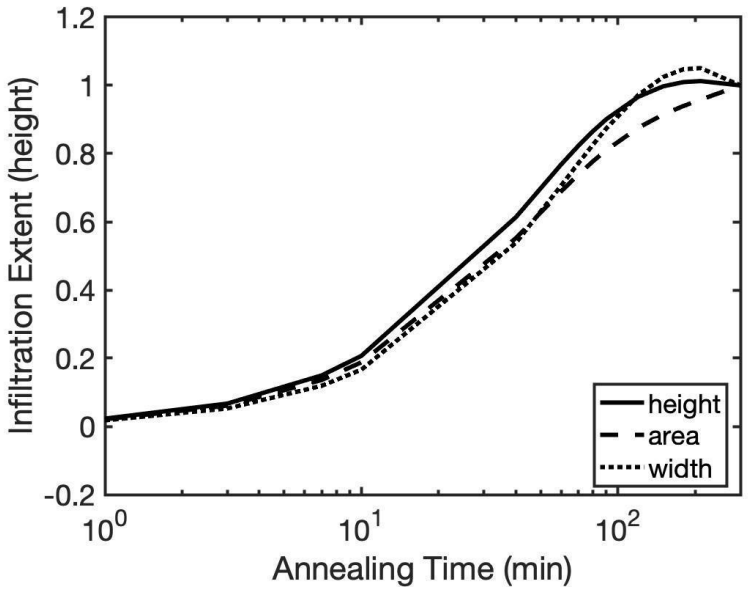

Figure S12: Infiltration extent vs annealing time of P2VP-547 composite.

DDA Simulation Details

The T-shape structure is defined in Cartesian coordinates and discretized into a cubic array of dipoles. The polarizability of each dipole is calculated by the Clausius-Mossotti relationship[1] as shown in Equation S1 below.

$$\alpha_i = \frac{3d^3}{4\pi}\left(\frac{\epsilon_i - 1}{\epsilon_i + 2}\right) \qquad \text{Equation S1}$$

where ϵ_i is the dielectric constant of dipole i, and d is the lattice constant. Equation S1 is further corrected by Draine and Goodman to the widely used lattice dispersion relation[2] as shown in Equation S2,

$$\alpha_i^{LDR} = \frac{\alpha_i}{1 + (\alpha_I/d^3)[(b_1 + n^2 b_2 + n^2 b_3 S)(kd)^2 - i(2/3)(kd)^3]} \qquad \text{Equation. S2}$$

where b_1=-1.891531, b_2=0.1648469, b_3=-1.770004, n is the refractive index, and S is a real number associated with the polarization of the incident radiation such that $S=\sum_{j=1}^{3}(\hat{\alpha}_j\hat{e}_j)^2$, where $\hat{\alpha}$ and $\hat{e}$ are unit vectors pointing in the propagation and polarization directions of the incident radiation.

Because the ligament diameter size is ca. 50 nm (AFM) is comparable to the mean free path of gold conduction electrons (42 nm at room temperature), the bulk dielectric constant fails to completely describe plasmon absorption in metals [3]. To account for this increase in electron collisions at nanoparticle surface, a correction to the dielectric constant is needed [3],

$$\varepsilon_{NP}(\omega, r_{eff}) = \varepsilon_{bulk}(\omega) + \frac{\omega_p^2}{\omega^2 + i\Gamma_0\omega} - \frac{\omega_p^2}{\omega^2 + i\Gamma(r_{eff})\omega} \qquad \text{Equation. S3}$$

where ε_{bulk} is the bulk dielectric constant at wavelengths from 400 to 800 nm obtained from Johnson and Christy [4], ω is the frequency of the incident light, $\omega_p = 1.35 \times 10^{16}\,\text{rad} \cdot \text{s}^{-1}$ is the gold plasma frequency [5], $\Gamma_0 = 1.07 \times 10^{14}\,\text{rad} \cdot \text{s}^{-1}$ is the electron collision frequency in bulk gold [5], $r_{eff} = (3V/4\pi)^{1/3}$ represents for the effective radius where $V=2\pi \times L \times r^2 - 8/3 \times r^3$ for the T-shape model, with r = 25 nm and L = 125 nm. $\Gamma(r_{eff})$ is the corrected collision frequency given by $\Gamma(r_{eff}) = \Gamma_0 + A\frac{V_F}{r_{eff}}$, where A = 1 is the empirical parameter for gold, and $V_F = 1.4 \times 10^6$ m/s is the Fermi velocity [6].

Because each dipole interacts with the incident electromagnetic field, the dipole moment and absorption coefficient can be determined from both re-radiating dipoles and the incident E field. The re-radiating dipoles are assumed to be instantaneously re-radiated given such small spacing between each dipole. Thus, the final electric field interacting with each dipole consists of

two components, $E_i = E_{inc} - \sum_{j \neq i} A_{ij} P_j$,where $P_j = \alpha_j E_j$ is the polarization of dipole j. The interaction tensor A_{ij} can be determined by an off-diagonal matrix according to the Green's tensor of electric field of radiation derived from the vector Helmholtz equation [2],

$$A_{jk} = \frac{\exp(ikr_{jk})}{r_{jk}} \times [k^2(\hat{r}_{jk}\hat{r}_{jk} - I_3) + \frac{ikr_{jk} - 1}{r_{jk}^2}(3\hat{r}_{jk}\hat{r}_{jk} - I_3)] \quad \text{Equation. S4}$$

where I_3 is the 3×3 identity matrix, $r_{jk} = |r_j - r_k|$, and $\hat{r}_{jk} = (r_j - r_k)/r_{jk}$.

The diagonal tensors for self radiation can be defined as the inversion of polarizability, $A_{jj} = \alpha_j^{-1}$. Thus, the original system of linear equations can be simplified as:

$$\sum_j A_{ij} P_j = E_{inc} \quad \text{Equation. S5}$$

which can be solved by standard numerical methods and used to obtain the dipole polarizability.

During polymer infiltration of the NPG, the medium starts as air, evolves to a bilayer of pure NPG over a mixture of NPG/P2VP and finally to NPG completely filled with P2VP. To represent the dielectric constant of the pores, effective medium approximation is used $n_{eff}^2 = (n_1^2 h_1 + n_2^2 h_2)/h$ [7], where $n_1 = 1.00$ and $n_2 = 1.54$ are the refractive index of air and P2VP accordingly, while h_2, h_1, and h are the thickness of the infiltrated NPG, unfilled NPG, and the total thickness of the NPG, 150 nm.

Finally, given polarizabilities of each dipole and the incident light electric field, the absorption (C_{abs}) and scattering (C_{sca}) cross sections can be calculated using [2],

$$C_{abs} = \frac{4\pi k}{|E_0|^2} \sum_{i=1}^{N} \{Im[P_i(\alpha_i^{-1})^* P_i^*] - \frac{2}{3}k^3 |P_i|^2\} \quad \text{Equation. S6}$$

$$C_{sca} = \frac{4\pi k}{|E_0|^2} \sum_{i=1}^{N} Im(E_i^* P_i) - C_{abs} \quad \text{Equation. S7}$$

where E_i^*, P_i^*, and α_i^* represent the complex conjugates of electric field, polarization and polarizability accordingly. The sum of two cross sections yields the extinction cross section, C_{ext}. The absorption, scattering, and extinction efficiency coefficients are defined below, and will be used for analysis in the result section.

$$Q_{abs} = \frac{C_{abs}}{\pi \alpha_{eff}^2} \quad \text{Equation. S8}$$

$$Q_{sca} = \frac{C_{sca}}{\pi \alpha_{eff}^2} \quad \text{Equation. S9}$$

$$Q_{ext} = Q_{abs} + Q_{sca} \quad \text{Equation. S10}$$

DDA: Au Rod Absorbance Spectra in air, water, and P2VP

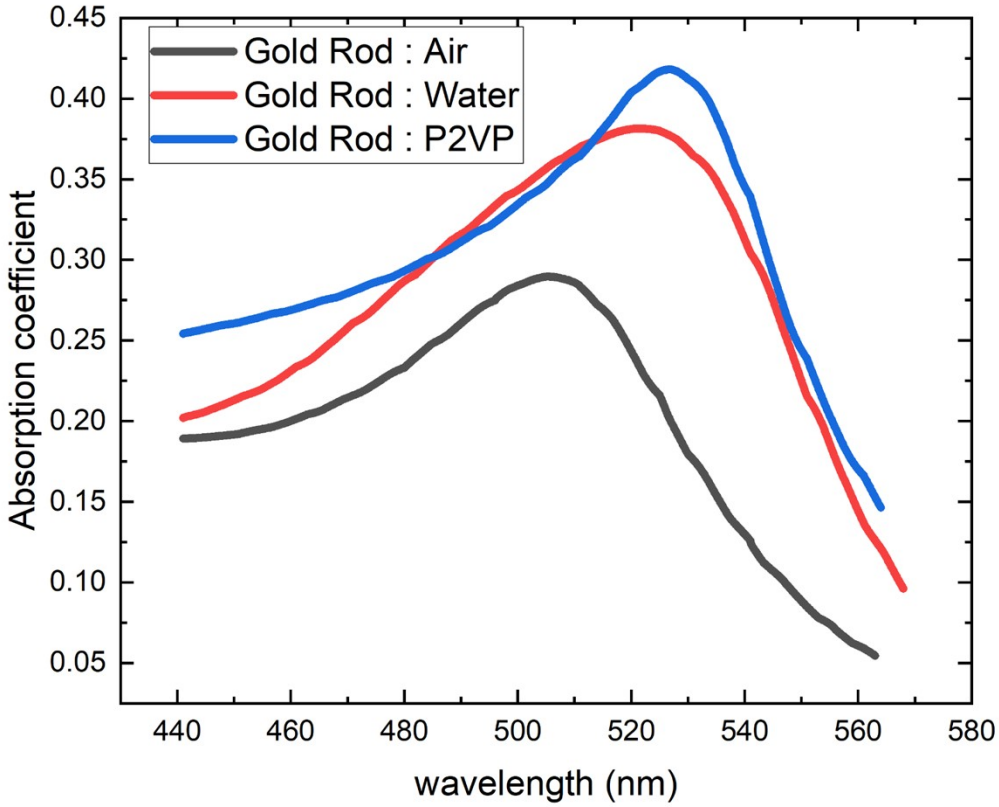

Figure S13. Gold Rod absorbance behavior in air, water and P2VP respectively.

DDA: Analysis on three different surrounding mediums

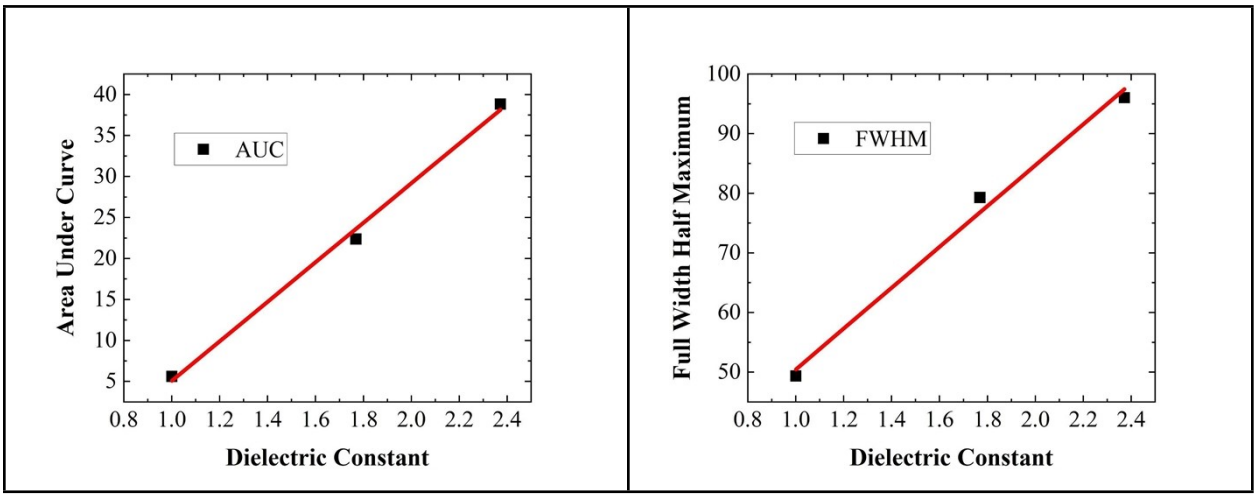

Figure S14. Relationships between (a) Area Under Curve (AUC) and (b) Full Width Half Maximum (FWHM) with dielectric constant, as the medium changes from air (n=1), water (n=1.33), to P2VP (n=1.54). Linear fitting with Pearson's r equal to (a) 0.99791, (b) 0.99573, and R-square(COD) equal to (a) 0.99582, (b) 0.99147.

DDA: Relationship of Infiltration Extent on Area Under Curve and Full Width Half Maximum

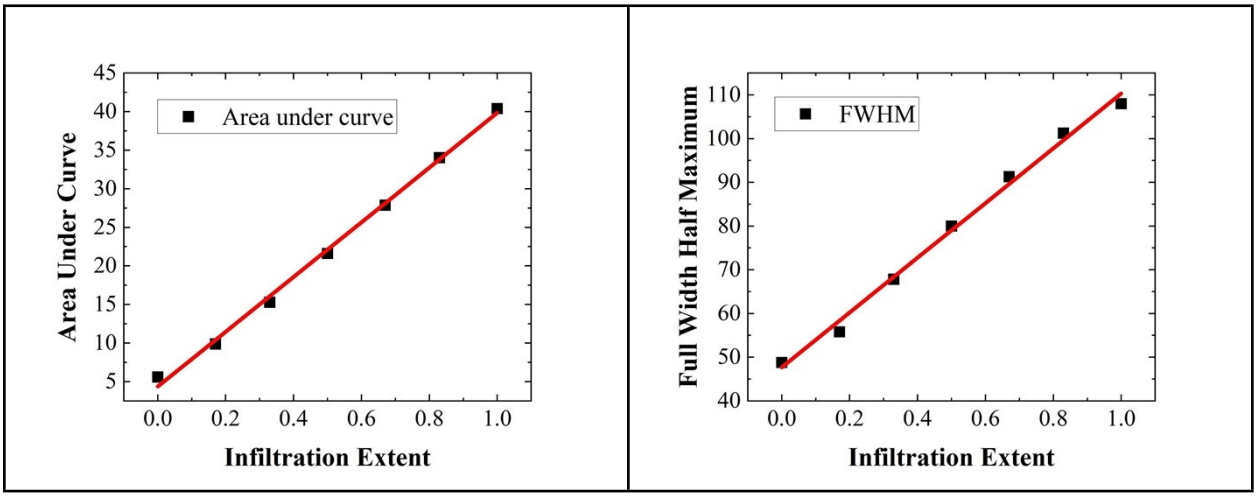

Figure S15. Area under curve and Full Width Half Maximum of NPG with different P2VP infiltration extents from DDA simulation. Linear fitting with Pearson's r equal to (a) 0.99843, (b) 0.9968, and R-square(COD) equal to (a) 0.99686, (b) 0.99361.

DDA: Calculated IE vs. IE for Area Under Curve and Full Width Half Maximum Analysis

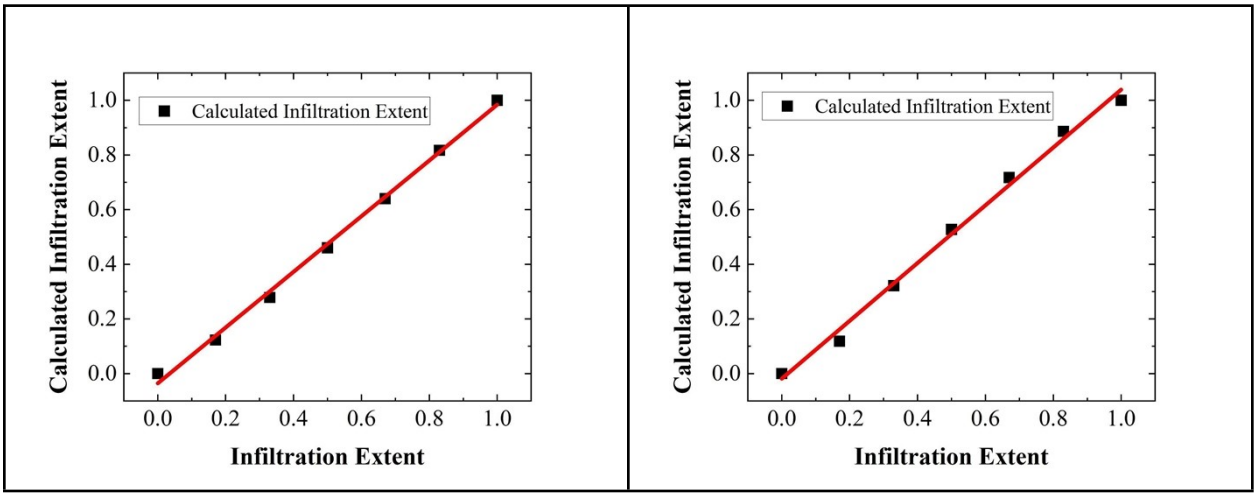

Figure S16. Plot of calculated infiltration extent from (a) area under curve and (b) full width half maximum vs. pre-defined infiltration extent. Slope of the linear fitting equal to (a) 1.01929, (b) 1.05831, with standard error of (a) 0.02558, (b) 0.03794

Reference

1. Purcell, E. M. & Pennypacker, C. R. Scattering and Absorption of Light by Nonspherical Dielectric Grains. *Astrophys. J.* **186**, 705 (1973).
2. Draine, B. T. & Flatau, P. J. Discrete-Dipole Approximation For Scattering Calculations. *J. Opt. Soc. Am. A* **11**, 1491 (1994).
3. Romann, J., Wei, J. & Pileni, M.-P. Computational Matching of Surface Plasmon Resonance: Interactions between Silver Nanoparticles and Ligands. *J. Phys. Chem. C* **119**, 11094–11099 (2015).
4. Johnson, P. B. & Christy, R. W. Optical Constants of the Noble Metals. *Phys. Rev. B* **6**, 4370–4379 (1972).
5. Genzel, L., Martin, T. P. & Kreibig, U. Dielectric function and plasma resonances of small metal particles. *Z. F□r Phys. B Condens. Matter Quanta* **21**, 339–346 (1975).
6. Ashcroft, N. W., Mermin, N. D. & Smoluchowski, R. *Solid State Physics*. *Phys. Today* **30**, 61–65 (1977).
7. El-Haija, A. J. A. Effective medium approximation for the effective optical constants of a bilayer and a multilayer structure based on the characteristic matrix technique. *J. Appl. Phys.* **93**, 2590–2594 (2003).